Characterization of $Ln_4Al_2O_9$ (Ln=Y, Sm, Eu, Gd, Tb) rare-earth aluminates as new high-temperature barriers

Aroa Morán-Ruiz (1), Karmele Vidal (1), Aitor Larrañaga (1), María Isabel Arriortua (1,2)*

(1) Universidad del País Vasco (UPV/EHU), Facultad de Ciencia y Tecnología, Departamento de Mineralogía y Petrología, Barrio Sarriena S/N, 48940 Leioa, Vizcaya, Spain.

(2) BCMaterials (Basque Centre for Materials, Applications & Nanostructures), Technological Park of Zamudio, Camino de Ibaizabal, Bndg. 500-1st, 48160, Derio, Spain.

Abstract

A family of cuspidine-type rare-earth aluminates with the general formula $Ln_4Al_2O_9$ (Ln= Y, Sm, Eu, Gd, Tb) has been prepared as a strategy to improve the thermal barrier coating (TBC) fulfilment. Varying trivalent lanthanides is applied to tailor the properties of oxides as ceramic top coats, for high temperature applications. After different heat treatments, X-ray diffraction (XRD) results concluded that $Eu_4Al_2O_9$ has the highest structural stability at 1200 and 1300 ºC. Moreover, the $Y_4Al_2O_9$ has a long lifetime at 1000 ºC and is stable at 1100 ºC. $Sm_4Al_2O_9$ and $Gd_4Al_2O_9$ showed higher stability at 1200 ºC than that of $Tb_4Al_2O_9$. However, terbium aluminate exhibited at 300-1000 ºC the highest thermal expansion coefficient. For five compositions thermal diffusivity measurements indicated favourable values at 600 ºC, which are lower than that of YSZ.

Keywords: Thermal barrier coatings; cuspidine-type rare-earth aluminates; X-ray powder diffraction; thermal diffusivity; thermal expansion coefficient.

---

*Corresponding author: Maribel Arriortua

E-mail address: maribel.arriortua@ehu.eus

Universidad del País Vasco (UPV/EHU), Facultad de Ciencia y Tecnología,
Departamento de Mineralogía y Petrología,
Barrio Sarriena S/N, 48940 Leioa, Vizcaya, Spain
Tel.: +34 946015984

1. Introduction

The use of thermal barriers is vital when an increase in a device operating temperature would result in an increase in efficiency [1]. Conventional thermal barrier coating (TBC) systems consist of three layers over the alloy substrate: (i) a metallic bond coat (BC), (ii) an intermediate thermally grown oxide (TGO) and, (iii) a ceramic top coat (TC). All these layers have different physical, mechanical, and thermal properties, which are strongly affected by the processing conditions [2]. The top coat is the outer layer that meets the hot working gases first, and is expected to thermally isolate the other TBC layers. The requirements of these ceramic barriers are: (i) high melting temperature, (ii) low thermal conductivity, (iii) thermal expansion coefficient (TEC) in line with the underlying alloy substrate, (iv) strain tolerance, (v) morphological and structural stability with temperature, (vi) resistance to oxidation and corrosion and, (vii) low cost [3, 4]. Up to now, the most successful TBC materials in use are 6-8% in wt. yttria stabilized zirconia oxides (YSZ: Y_2O_3-ZrO_2). They have sufficient porosity and microstructural defects to reduce their thermal conductivity and make them compliant in accommodating thermal strain. However, YSZ coatings undergo enhanced sintering and phase transformation at high temperatures (> 1200 ºC). The decomposition of tetragonal zirconia with the formation of monoclinic or cubic phase is usually accompanied by volume change and extended cracking. Thus, there is a need for TBCs that combine all of the desirable attributes of 6-8YSZ and, at the same time address the above critical issues [5-13].

Rare earth (RE) zirconate pyrochlores have received intense interest due to their low thermal conductivity and high phase stability. However, the interaction between pyrochlores and TGO may reduce the durability of the system. Moreover, the study of thermochemical compatibility of $GdO_{1.5}$-ZrO_2 compositions with thermally grown oxide (Al_2O_3) resulted in the formation of $GdAlO_3$ interphase [3]. This gives a useful compositional design guideline for TBC materials. Therefore, the use of materials based on zirconia (ZrO_2) stabilized with rare and/or alkaline earth oxides (Pr_2O_3, Nd_2O_3, Sm_2O_3, CeO_2, CaO, MgO, etc.) as thermal barriers would be interesting. Additionally, co-doping YSZ with trivalent rare earth is considered as one of the effective ways to develop alternative ceramic materials with high phase stability and low thermal conductivity. This will be extended to non-metal dopants; recent preliminary works

have shown the ability of these fluorite-type systems to accommodate low levels (up to 5 mol%) of phosphate [14]. As part of the attempts to discover alternative structures, a new family of high thermal stability materials derived from cuspidine structure has been recently reported [15, 16]. Minerals of the cuspidine group can be described with the general formula $Ln_4Al_2O_9$, where Ln is a trivalent lanthanide. The archetype compound of cuspidine family is, $Y_4Al_2O_9$ (YAM), which crystallises in the space group $P2_1/c$. According to previous studies, $Y_4Al_2O_9$ showed a reversible thermal phase transformation from low temperature monoclinic to high temperature monoclinic phase at 1377 ºC [17]. Here, we report the synthesis and characterization of new oxides based on cuspidine-type rare-earth aluminates, $Ln_4Al_2O_9$ (Ln= Y, Sm, Eu, Gd, Tb). Combustion method was used to prepare analogues of $Y_4Al_2O_9$ to study their microstructure, structural stability, thermal diffusivity and, thermal expansion behaviour.

2. Experimental

$Ln_4Al_2O_9$ (Ln=Y, Sm, Eu, Gd, Tb) samples were prepared by the glycine nitrate combustion (GNC) route, under identical synthetic conditions, in order to study the influence of varying trivalent lanthanides, in the context of their applications as a thermal barrier for high-temperature applications. The synthesis of the samples was performed using $Y(NO_3)_3{\cdot}6H_2O$ (99.8%), $Gd(NO_3)_3{\cdot}6H_2O$ (99.9%), $Eu(NO_3)_3{\cdot}5H_2O$ (99.9%), $Sm(NO_3)_3{\cdot}6H_2O$ (99.9%), $Tb(NO_3)_3{\cdot}5H_2O$ (99.9%) and $Al(NO_3)_3{\cdot}9H_2O$ (98%) as metal precursors and glycine (>99%) as combustion fuel, all from Aldrich. The glycine was added to obtain a fuel/oxidizer molar ratio of 1. The details of the synthesis were reported elsewhere. The resulting powders were calcined in air at 900 ºC for 8 h to obtain the pure samples.

All metal contents were determined by inductively coupled plasma atomic emission spectroscopy (ICP-AES) on a Horiba Yobin Yvon Activa spectrophotometer. For this purpose, samples were dissolved using a mixture of HNO_3 and HCl for one day to obtain a clear and measurable solution.

The structural analysis of the synthesized materials and, the characterization of the crystalline phases from all heated samples for 10 h, in the 1000-1300 ºC temperature range each 100 ºC, were performed using laboratory X-ray diffraction (XRD). Data

were collected at room temperature using a Philips X´Pert-Pro diffractometer, with Cu Kα radiation (λ= 1.5418 Å), from 2θ 5 to 80º, with a step size of 0.026º and 10 s per step. The power generator has been provided at 40 kV and 40 mA. Full-profile Rietveld refinements were performed using the FullProf program to get structural parameters of the identified phases and % in weight of each phase in the samples. For all the samples $Ln_4Al_2O_9$, the space group used for refinement was $P2_1/c$ (14). X-ray diffraction at high temperature, in situ, heating-cooling cycles at 1000 ºC and, thermodiffractometry (TDX) analysis of the obtained powders were carried out in a Bruker D8 Advance Theta-Theta diffractometer with Cu Kα radiation (λ=1.5418 Å) and HTK2000 chamber with a Pt sample holder. The power generator was set to 30 kV and 20 mA. For the TDX analysis, the patterns were recorded from room temperature to 1300 ºC each 20 ºC, which were scanned with 2 s ranging from 20-80 with 0.03º steps.

The morphology of the samples was determined using a scanning electron microscope (JEOL JSM-7000F). Secondary electron images were taken at 20 kV and $1.1 \cdot 10^{-11}$ A.

The $Ln_4Al_2O_9$ pellets were sintered at 1000 ºC for 10 h to achieve corresponding bulk samples. A laser flash apparatus (the Netzsch LFA 457 microflash) was used to measure thermal diffusivity from room temperature to 600 ºC, by Parker´s method; the sample size was about φ 12.7x2.5 mm. The thermal expansion coefficient of the bulk samples was tested by a Unitherm Model 1161 dilatometer, in the temperature range of 30-1000 ºC, being the size of the thermal expansion specimen about 1 x 3 x 7 mm.

3. Results and discussion

3.1. Phase characterization

Room temperature X-ray diffraction patterns of all synthesised $Ln_4Al_2O_9$ oxides are shown in Figure 1. The patterns reveal that all the samples are single-phase without impurities. Rietveld fits for the powder X-ray diffraction data were carried out using the monoclinic ($P2_1/c$) space group, the same structure observed for cuspidine mineral. The cell volumes of these compounds (Table 1), at room temperature, increased slightly with the ionic radius of the trivalent rare-earth elements: $Sm^{3+}>Eu^{3+}>Gd^{3+}>Tb^{3+}>Y^{3+}$ [18].

Results from chemical analyses, presented in Table 1, show a good agreement between the analysed chemical compositions of the prepared powders and the nominal compositions.

Figure 1

Table 1

Figure 2 presents the different morphologies of the prepared rare earth aluminate powders, as an example for $Eu_4Al_2O_9$ and $Gd_4Al_2O_9$, after heat treatment at 900 ºC. The micrographs for $Y_4Al_2O_9$, $Sm_4Al_2O_9$ and $Tb_4Al_2O_9$ are given as supplementary material (Figures S1). The observation of the different compositions by scanning electronic microscopy suggests identical microscopic characteristics between the five rare earths used. We can notice that all the powders are composed of agglomerated submicron particles with similar spongy morphology. Therefore, these microstructures depend more on the synthesis method than the composition. The aggregation rate is determined by the temperature generated during the combustion reaction that is higher in the fuel-rich case. Moreover, the agglomerates formed at lower G/N ratio are soft and could be easily split up, while those at the higher ratio are hard and difficult to break into particles [19]. In this work, the powders were prepared using an intermediate G/N value: 1. In this sense, it is expected to exhibit interesting pore morphologies to avoid enhanced sintering and, also to facilitate the formulation of stable slurries for deposition process.

SEM micrographs taken of the surface of the sintered bars at 1000 ºC, in air for 10 h, are also shown in Figure 2. The observed microstructures present similar pore morphology with submicron grain sizes. After sintering at 1000 ºC for 10 h, the relative densities of 64.03%, 58.42%, 55.25%, 52.97% and 48.75% of the theoretical value (obtained by XRD) were obtained for the $Tb_4Al_2O_9$ (TbAM), $Gd_4Al_2O_9$ (GdAM), $Sm_4Al_2O_9$ (SmAM), $Eu_4Al_2O_9$ (EuAM) and $Y_4Al_2O_9$ (YAM), respectively.

Figure 2

3.2. Phase thermal behaviour

3.2.1. Structural stability

The obtained degradation phases for the samples were identified and quantified after heat-treated for 10 h, in the 1000-1300 ºC temperature range each 100 ºC, and for prolonged exposure, 200 h, at 1000 ºC to establish the stability of the samples at each temperature and with the time. The results obtained by the Rietveld method are provided in Tables 2 and 3.

Tables 2 and 3

As an example, for $Eu_4Al_2O_9$ and $Gd_4Al_2O_9$, the calculated and difference X-ray powder diffraction patterns after different heat treatments are given in Figures 3-5. The corresponding Rietveld refinements of $Y_4Al_2O_9$, $Sm_4Al_2O_9$, and $Tb_4Al_2O_9$ are displayed as Supplementary material (Figures S2-S5).

Figures 3-5

$Y_4Al_2O_9$ is the most stable material at 1100 ºC. However, the formation of $YAlO_3$ (P*bnm*) orthorhombic perovskite and Y_2O_3 (I*a-3*) cubic oxide is observed at 1200 and 1300 ºC. In contrast, for $Eu_4Al_2O_9$ at 1100 ºC, the $EuAlO_3$ (P*bnm*) 3.7% in wt. is quantified and, at higher temperatures is stable. For $Gd_4Al_2O_9$ at 1100 ºC the formation of $GdAlO_3$ (P*bnm*) 7.9% in wt. is given. At 1200 ºC as main phase was identified: $Gd_4Al_2O_9$ (P$2_1/c$) 75.1% in wt. and, as secondary phases: $GdAlO_3$ (P*bnm*) 15.6% in wt. and Gd_2O_3 (C*2/m*) 9.3% in wt. However, the obtained results at 1300 ºC showed as the main phase $GdAlO_3$ (Pbnm) 41.8% in wt. and, as secondary phases: $Gd_4Al_2O_9$ (P$2_1/c$) 24.9% in wt. and Gd_2O_3 (C*2/m*) 33.3% in wt. Moreover, for $Tb_4Al_2O_9$ sample, at 1100 ºC, the $TbAlO_3$ (P*bnm*) 10% in wt. is formed. The results at 1200 ºC revealed that the main and secondary phases are $TbAlO_3$ (P*bnm*) 45.6% in wt. and Tb_2O_3 (C*2/m*) 34.3% in wt., Tb_2O_3 (I*a-3*) 17.0% in wt., $Tb_4Al_2O_9$ (P$2_1/c$) 3.1% in wt., respectively. At 1300 ºC, the composition of the formed phases has a similar trend to that at 1200 ºC (see Table 2). The material in which samarium is used showed the lowest thermal structural stability at 1100 ºC, in which as secondary phases $SmAlO_3$ (P*bnm*) 18.0% in wt. and Sm_2O_3 (C*2/m*) 10.3% in wt. are observed (see Table 2). However, samarium aluminate showed higher stability than that of $Tb_4Al_2O_4$ at 1200 and 1300 ºC (see Table 2).

The structural stability with respect to time increases in the following order: YAM>EuAM>GdAM>TbAM>SmAM. For the prepared $Ln_4Al_2O_9$ compounds, with the exception of $Y_4Al_2O_9$ that is stable over time, the corresponding $LnAlO_3$ (P*bnm*) phases are quantified (see Table 3).

Since the phase structure lifetime is crucial to the application of advanced thermal barrier coatings, a thermal cyclic test for $Y_4Al_2O_9$ was performed. Results showed that $Y_4Al_2O_9$ structure remains quite stable after 100 cycles of heating at 1000 ºC and cooling to room temperature (Figure 6). Considering $Y_4Al_2O_9$ as representative structure of the obtained $Ln_4Al_2O_9$ phases, the same results could expect for all the samples.

Figure 6

According to the obtained results, $Eu_4Al_2O_9$ has the highest structural stability at 1200 and 1300 ºC. The $Y_4Al_2O_9$ has a long lifetime at 1000 ºC and, promising structure stability at 1100 ºC. However, the phase instability of the $Y_4Al_2O_9$ and $Tb_4Al_2O_9$ at 1200 and 1300 ºC could affect the thermal shock resistance of these coatings [20]. Nevertheless, $Sm_4Al_2O_9$ and $Gd_4Al_2O_9$ show an intermediate stability at 1200 ºC.

The structural thermal stability was also studied by powder X-ray thermo-diffraction (TDX), in air, from room temperature to 1300 ºC. As an example, diffraction patterns of $Eu_4Al_2O_9$ and $Ga_4Al_2O_9$, measured from room temperature to high temperature each 20 ºC, as a dynamic process, are summarized in Figure 7. The TDX data for YAM, SmAM and TbAM are given as supplementary material (Figure S6). All the prepared samples are quite stable up to 1300 ºC, whereas the stability of samarium aluminate is relatively lower than that of the others. So that, the secondary phases formation occurs when the prepared samples heat for 10h to a given temperature, but not in situ high temperature measurements. Hence, the process of forming impurities depends on the temperature and greatly on heating time.

Figure 7

The variation of the $Ln_4Al_2O_9$ unit cell volumes from 900 to 1300 ºC each 100 ºC, which were obtained by full-profile refinement without structural model (Pattern matching), are illustrated in Figure 8.

Figure 8

For all samples, from ~1000 ºC on, the unit cell volumes did not show the same trend that at lower temperatures. These significant differences in the cell parameters could be explained by a thermal phase transformation from low monoclinic to high monoclinic phase. Several studies revealed that this reversible phase transitions in $Y_4Al_2O_9$ and other rare-earth aluminates $Ln_4Al_2O_9$ above 1000 ºC; these phase transitions have thermal hysteresis and a volume decrease of about %0.5 on heating from the low temperature phase to the high temperature phase. The calculated $Ln_4Al_2O_9$ unit cell volumes in the obtained residues, which are provided from the pattern matching refinements, indicated a high probability that the phase transition was reversible (see Table 4), in good agreement with bibliography [17].

Table 4

3.2.2. Thermal diffusivity

Thermal diffusivity values for the obtained materials heat-treated for 10h at 1000 ºC are shown in Figure 9. The microstructure of the compounds influences the thermal diffusivity because of the effects of the grain growth and sintering behaviours. The microstructures of the measured samples are detailed, previously, in phase characterization section.

Figure 9

As shown in Figure 9, for all the samples, the thermal diffusivity decreases with increasing of temperature ranges from room temperature to 600 ºC, which suggests a typical phonon thermal conduction behaviour in the measuring temperature range. From room temperature to 600 ºC, the thermal diffusivity of YAM, SmAM, EuAM, GdAM and TbAM lie in a range of 0.37-0.30, 0.40-0.28, 0.34-0.27, 0.38-0.30 and 0.40-0.28 mm^2/s, respectively. These values are lower than that of several oxide type materials that have been studied as top coating in TBC production, such as, La_3TaO_7, La_2AlTaO_7 and, the most used Y_2O_3-doped ZrO_2 (YSZ) [5, 7, 21].

Therefore, the obtained thermal diffusivity results for the prepared $Ln_4Al_2O_9$ compounds indicated better thermal insulation as compared to recently studied many types of rare earth element based oxides.

3.2.3. Thermal expansion coefficient

Figure 10 shows the thermal expansion curves of the prepared five materials obtained upon heating from 300 to 1000 ºC. As shown in Figure 10, all the samples exhibit the same behaviour: an increase in temperature results in the expansion of the structure.

Figure10

The average TECs at 300-1000 ºC for the synthesized $Ln_4Al_2O_9$ oxides are listed in the Table 5.

Table 5

The values of thermal expansion increased from 7.7 to $11.8 \cdot 10^{-6}$ K^{-1} in the following order: GdAM<EuAM<YAM<SmAM<TbAM, which are comparable to those of widely used ceramics for thermal barrier coatings applications [6, 8, 22, 23]. $Tb_4Al_2O_9$ has the largest TEC that is comparable to that of Y_2O_3 (7.8% in wt.) stabilized ZrO_2.

High TEC is necessitated for TBC materials to reduce the thermal expansion mismatch between the ceramic coating and the substrate. Hence, lower thermal expansion coefficients may lead to higher stress generation during thermal cycling.

4. Conclusions

The cuspidines $Ln_4Al_2O_9$ (Ln=Y, Sm, Eu, Gd, Tb) have been satisfactorily prepared, using glycine/nitrate in a one ratio, as thermal barrier top coatings. At room temperature, all compounds showed monoclinic symmetry ($P2_1/c$). They showed similar pore morphology with submicron grain size after sintering at 1000 ºC and, favourable thermal diffusivity at 600 ºC, which is lower than that of YSZ. Furthermore, $Eu_4Al_2O_9$ has a high structural stability at 1200 and 1300 ºC. Moreover, the $Y_4Al_2O_9$ has a long lifetime at 1000 ºC and, promising structure stability at 1100 ºC. However, the phase instability of the $Y_4Al_2O_9$ and $Tb_4Al_2O_9$ materials at 1200 and 1300 ºC could lead to microstructural changes resulting in higher thermal stress generation. Nevertheless,

$Sm_4Al_2O_9$ and $Gd_4Al_2O_9$ showed an intermediate phase stability at 1200 ºC. Samarium aluminate is more stable than that gadolinium aluminate at 1300 ºC.

The low thermal expansion coefficient of $Gd_4Al_2O_9$ is a disadvantage of this material with respect to the studied others. In this sense, $Tb_4Al_2O_9$ exhibited at 300-1000 ºC the highest TEC as compared with standard YSZ that is the most used in TBC production.

Acknowledgements

This research has been funded by the Ministerio de Economía, Industria y Competitividad (MAT2016-76739-R) (AEI/FEDER, UE), and Departamento de Educación of the Basque Government (IT-630-13). The authors thank SGIker of UPV/EHU for technical and personnel support. A. Morán-Ruiz thanks UPV/EHU for funding.

Appendix A. Supplementary material

References

[1] V. Stathopoulos, V. Sadykov, S. Pavlova, Y. Bespalko, Y. Fedorova, L. Bobrova, A. Salanov, A. Ishchenko, V. Stoyanovsky, T. Larina, V. Ulianitsky, Z. Vinokurov, V. Kriventsov, Design of functionally graded multilayer thermal barrier coatings for gas turbine application, Surf. Coat. Technol. 295 (2016) 20-28.

[2] A.C. Karaoglanli, K. Ogawa, A. Turk, I. Ozdemir, Thermal shock and cycling behaviour of thermal barrier coatings (TBCs) used in gas turbines, in: E. Benini (Ed.), Progress in gas turbine performance, InTech, 2013.

[3] V. Kumar, B. Kandasubramanian, Processing and design methodologies for advanced and novel thermal barrier coatings for engineering applications, Particuology (2016) 1-28.

[4] D.L. Poerschke, C.G. Levi, Effects of cation substitution and temperature on the interaction between thermal barrier oxides and molten CMAS, J. Eur. Ceram. Soc. 35 (2015) 681-691.

[5] L. Sun, H. Guo, H. Peng, S. Gong, H. Xu, Influence of partial substitution of Sc_2O_3 with Gd_2O_3 on the phase stability and thermal conductivity of Sc_2O_3-doped ZrO_2, Ceram. Int. 39 (2013) 3447-3451.

[6] L. Guo, M. Li, Y. Zhang, F. Ye, Improved toughness and thermal expansion of non-stoichiometry $Gd_{2-x}Zr_{2+x}O_{7+x/2}$ ceramics for thermal barrier coating application, J. Mater. Sci. Technol. 32 (2016) 28-33.

[7] L. Guo, M. Li, F. Ye, Phase stability and thermal conductivity of RE_2O_3 (RE=La, Nd, Gd, Yb) and Yb_2O_3 co-doped Y_2O_3 stabilized ZrO_2 ceramics, Ceram. Int. 42 (2016) 7360-7365.

[8] J. Fenech, M. Dalbin, A. Barnabe, J.P. Bonino, F. Ansart, Sol-gel processing and characterization of (RE-Y)-zirconia powders for thermal barrier coatings, Powder Technol. 208 (2011) 480-487.

[9] X. Wang, S. Guo, L. Zhao, Y. Zhu, L. Ai, A novel thermal barrier coating for high temperature applications, Ceram. Int. 42 (2016) 2648-2653.

[10] S.M. Naga, A.M. Hassan, H.F. El-Maghraby, M. Awaad, H. Elsayed, In-situ sintering reaction of Al_2O_3-$LaAl_{11}O_{18}$-ZrO_2 composite, Int. J. Refract. Met. Hard Mater. 54 (2016) 230-236.

[11] M.R. Loghman-Estarki, R. Shoja-Razavi, H. Edris, S.R. Bakhshi, M. Nejati, H. Jamali, Comparison of hot corrosion behaviour of nanostructured ScYSZ and YSZ thermal barrier coatings, Ceram. Int. 42 (2016) 7432-7439.

[12] M.R. Loghman-Estarki, R. Shoja-Razavi, H. Jamali, R. Ashiri, Effect of scandia content on the thermal shock behaviour of SYSZ thermal sprayed barrier coatings, Ceram. Int. 42 (2016) 11118-11125.

[13] N.P. Padture, Advanced structural ceramics in aerospace propulsion, Nat. Mater. 15 (2016) 804-809.

[14] A.D. Smith, J.F. Shin, P.R. Slater, Synthesis and characterization of oxyanion (phosphate, sulphate) doped $Ba_2Sc_{2-y}Ga_yO_5$, J. Solid State Chem. 198 (2013) 247-252.

[15] M.C. Martín-Sedeño, D. Marrero-López, E.R. Losilla, S. Bruque, P. Núñez, M.A.G. Aranda, Stability and oxide ion conductivity in rare-earth aluminium cuspidines, J. Solid State Chem. 179 (2006) 3445-3455.

[16] X. Zhou, Z. Xu, X. Fan, S. Zhao, X. Cao, L. He, $Y_4Al_2O_9$ ceramics as a novel thermal barrier coating material for high-temperature applications, Mater. Lett. 134 (2014) 146-148.

[17] H. Yamane, M. Shimada, High-temperature neutron diffraction study of $Y_4Al_2O_9$, J. Solid State Chem. 141 (1998) 466-474.

[18] J. Dohrup, A. Hoyvald, G. Mogensen, J.H. Jacobsen, J. Villadsen, Formation of new compounds $Ln_4Al_2O_9$ in the $Ln_2O_3 \cdot Al_2O_3$ system (Ln= La, Pr, Tb), J. Am. Ceram. Soc. 79(11) (1996) 2959-2960.

[19] K. Vidal, A. Larrañaga, A. Morán-Ruiz, M.A. Laguna-Bercero, R.T. Baker, M.I. Arriortua, Effect of the synthesis conditions on the properties of $La_{0.15}Sm_{0.35}Sr_{0.08}Ba_{0.42}FeO_{3-\delta}$ cathode material for SOFCs, Powder Technol. 322 (2017) 131-139.

[20] S. Ghosh, Thermal barrier ceramic coatings-a review, in: A.M.A. Mohamed (Ed.), Advanced ceramic processing, InTech, 2015.

[21] Z. Haoming, F. Yan, C. Xiaoge, Z. Hongsong, L. Yanxu, T. An, R. Bo, Thermal properties of La3TaO7 and La2AlTaO7 oxides, Ceram. Int. 43 (2017) 755-759.

[22] R. Vassen, X. Cao, F. Tietz, D. Basu, D. Stöver, Zirconates as new materials for thermal barrier coatings, J. Am. Ceram. Soc. 83(8) (2000) 2023-2028.

[23] J. Wu, X. Wei, N.P. Padture, P.G. Klemens, M. Gell, E. García, P. Miranzo, M.I. Osendi, Low-thermal-conductivity rare-earth zirconates for potential thermal-barrier-coating applications, J. Am. Ceram. Soc. 85(12) (2002) 3031-3035.

Figure Captions and Tables

Figure 1. Rietveld X-ray diffraction pattern refinements for the prepared $Y_4Al_2O_9$, $Sm_4Al_2O_9$, $Eu_4Al_2O_9$, $Gd_4Al_2O_9$ and $Tb_4Al_2O_9$ oxides. Circles denote experimental points; upper solid line the calculated profile. Theoretical peak positions (vertical sticks) and difference lines are shown in the bottom of each pattern.

Figure 2. Micrographs of $Eu_4Al_2O_9$ and $Ga_4Al_2O_9$ oxides obtained by combustion method and, after sintering at 900 and 1000 ºC, in air.

Figure 3. X-ray diffraction pattern refinements performed in the obtained $Eu_4Al_2O_9$ cuspidine-type oxide after heating at different temperatures.

Figure 4. X-ray diffraction pattern refinements performed in the obtained $Gd_4Al_2O_9$ cuspidine-type oxide after heating at different temperatures.

Figure 5. Rietveld refinements of the $Eu_4Al_2O_9$ and $Gd_4Al_2O_9$ samples after heating at 1000 ºC for 200h.

Figure 6. Results of $Y_4Al_2O_9$ phase net area (Cps·2θº) and FWHM (2θº) after 100 cycles at 1000 ºC, in air.

Figure 7. Diffraction patterns of $Eu_4Al_2O_9$ and $Gd_4Al_2O_9$ measured from room temperature to 1300 ºC, each 100 ºC, as a dynamic process. The diffractogram of the corresponding residue is also included.

Figure 8. The variation of unit cell volumes of the prepared $Ln_4Al_2O_9$ cuspidine-type oxides from 900 to 1300 ºC, each 100 ºC.

Figure 9. Thermal diffusivity of the prepared Ln4Al2O9 (Ln= Y, Sm, Eu, Gd, Tb) samples as a function of temperature.

Figure 10. Thermal expansion curves of the prepared samples, obtained upon heating from 300 to 1000 ºC in air.

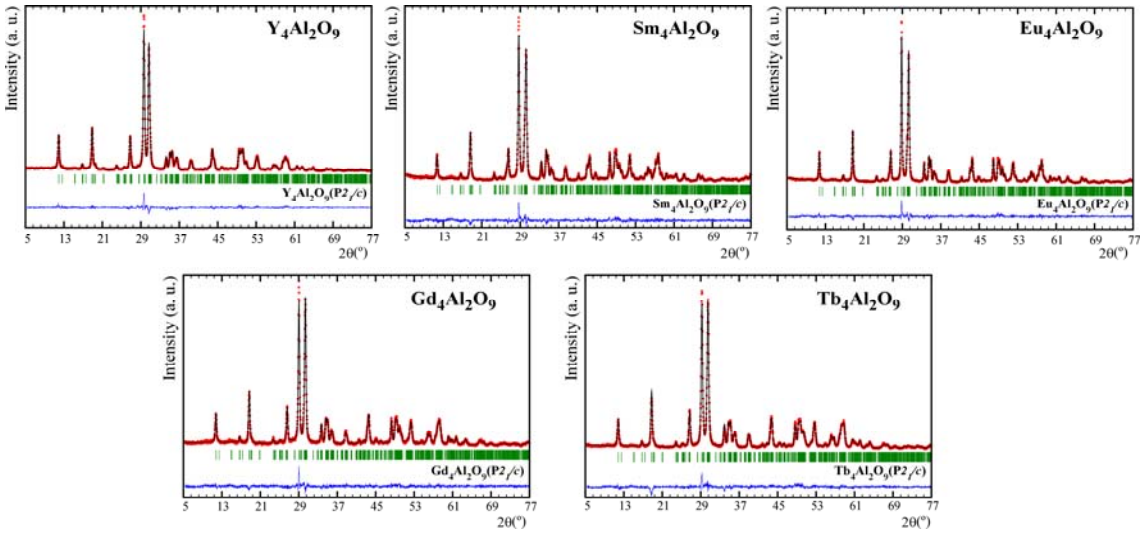

Figure 1

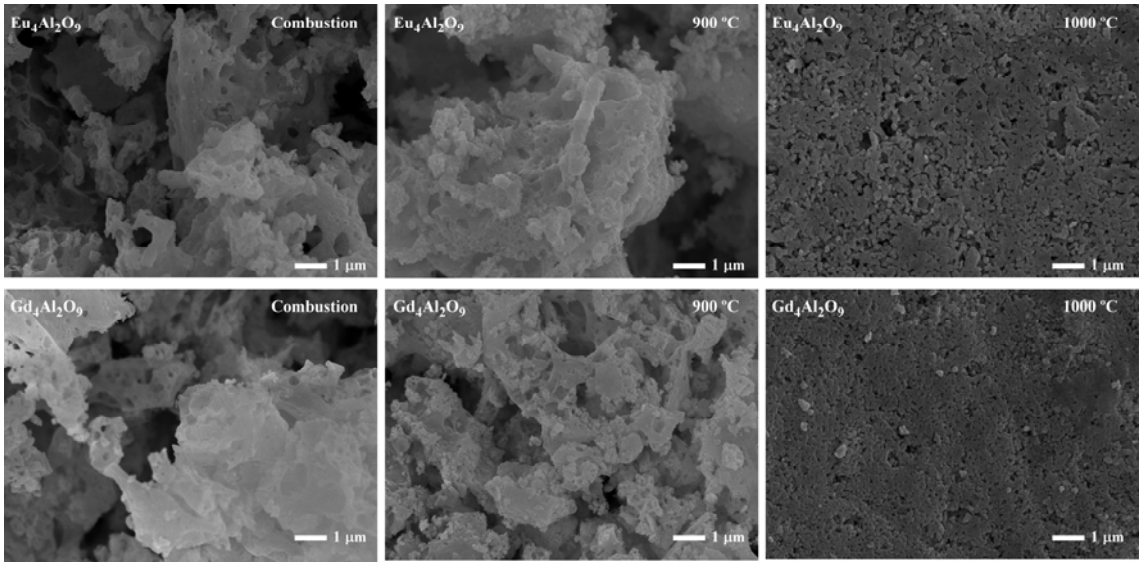

Figure 2

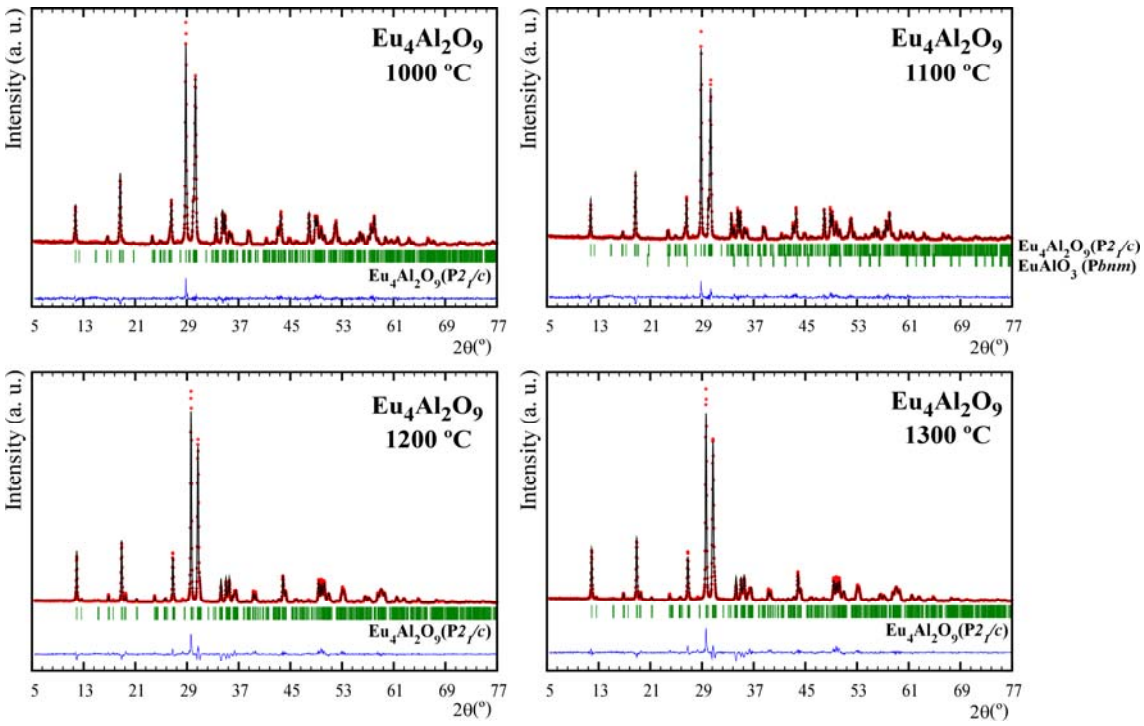

Figure 3

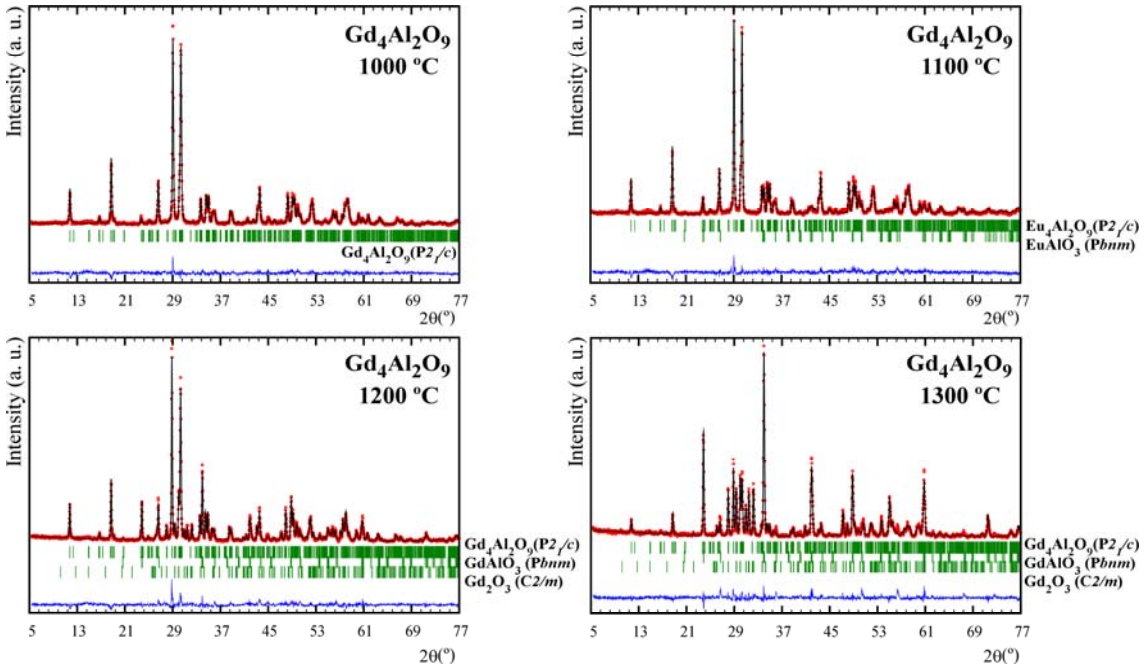

Figure 4

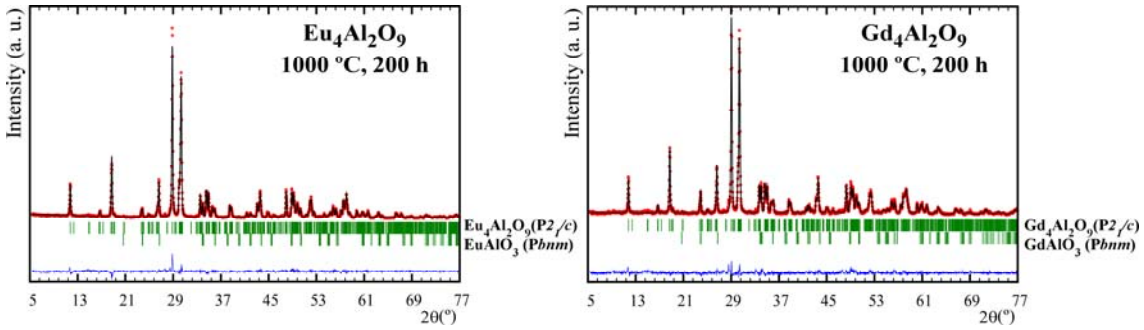

Figure 5

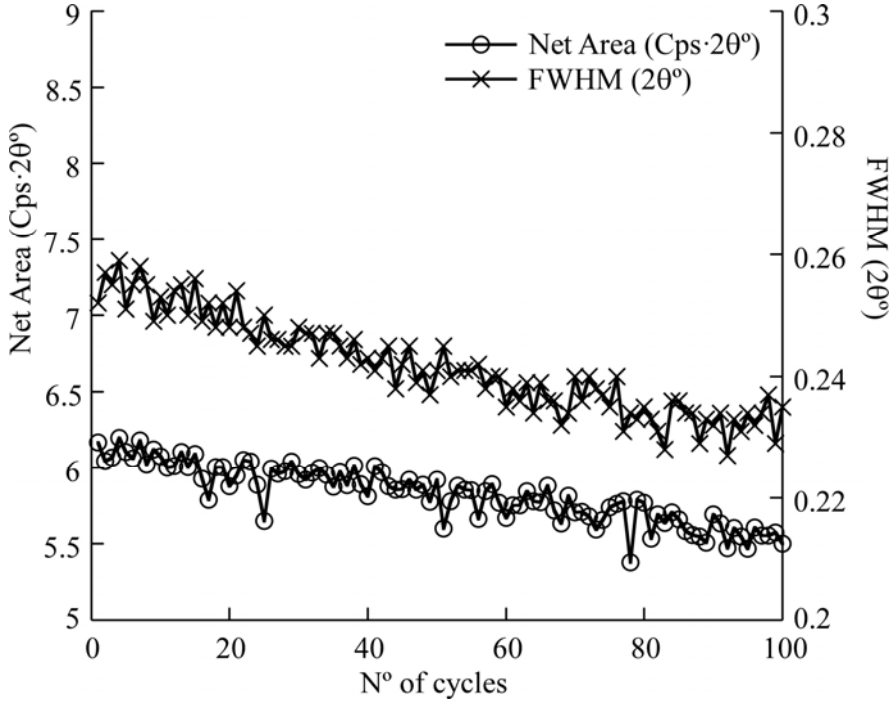

Figure 6

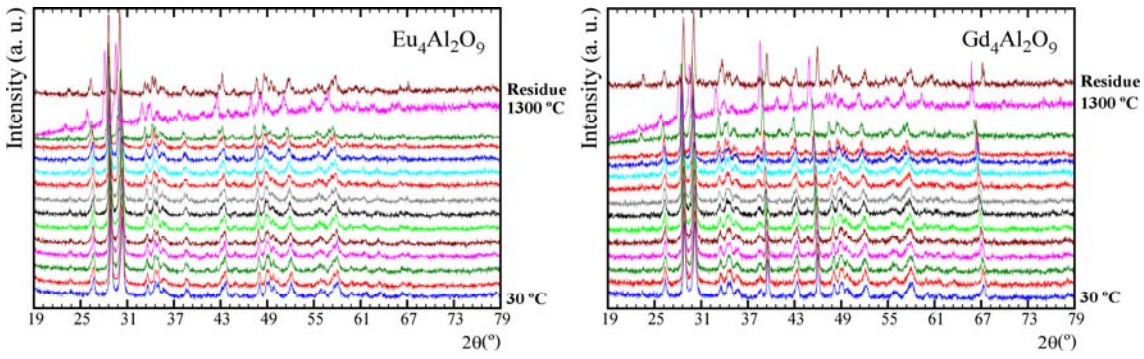

Figure 7

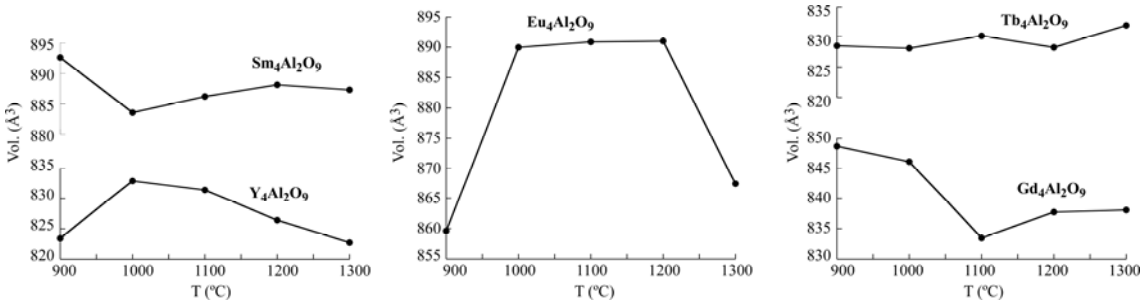

Figure 8

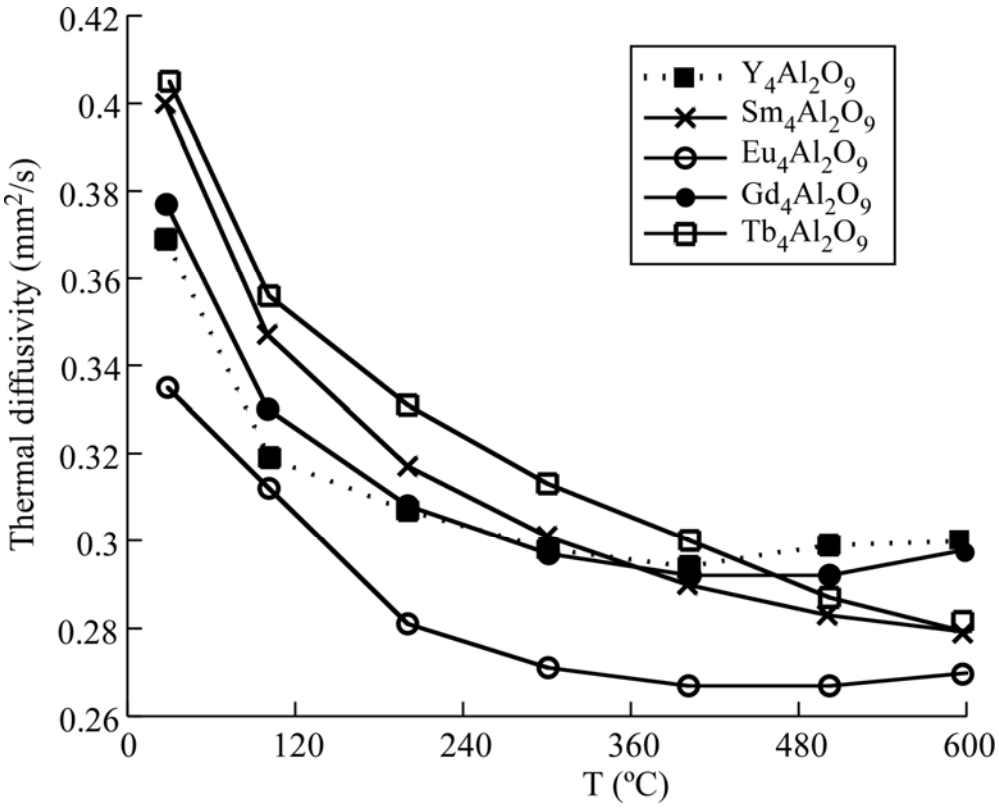

Figure 9

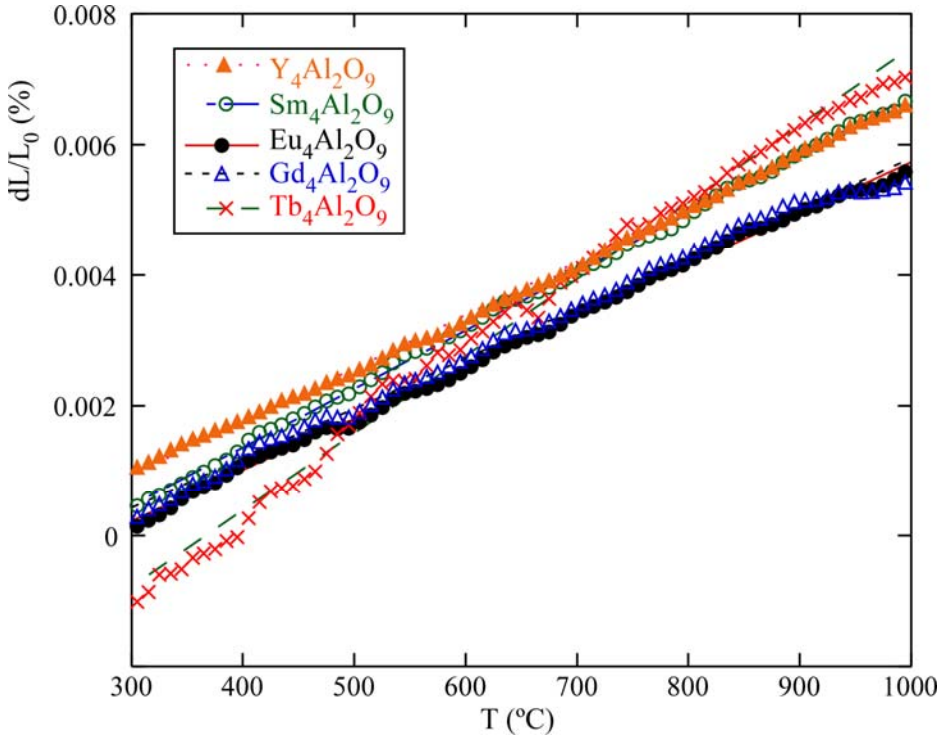

Figure 10

Table 1. Summary of the ICP results and the obtained cell volumes from the Rietveld analysis of the $Ln_4Al_2O_9$ cuspidine-type oxides.

Table 2. Rietveld results, % in weight of the formed phases in the obtained $Ln_4Al_2O_9$ pure powders after heating at different temperatures.

Table 3. Rietveld results, % in weight of the identified phases in the prepared $Ln_4Al_2O_9$ powders after sintering at 1000 ºC for 200h.

Table 4. Comparison between the calculated initial and residue cell volumes for all the prepared samples at room temperature.

Table 5. Thermal expansion coefficients for the studied materials.

Table 1

Compound	*Chemical analysis*	*Structural analysis V(Å^3)*
$Sm_4Al_2O_9$	$Sm_{3.92(1)}Al_{2.06(1)}O_9$	868.90±0.1
$Eu_4Al_2O_9$	$Eu_{3.88(1)}Al_{2.12(1)}O_9$	857.99±0.1
$Gd_4Al_2O_9$	$Gd_{3.88(1)}Al_{2.12(1)}O_9$	849.28±0.1
$Tb_4Al_2O_9$	$Tb_{3.97(1)}Al_{2.18(1)}O_9$	835.20±0.1
$Y_4Al_2O_9$	$Y_{3.88(1)}Al_{2.06(1)}O_9$	812.58±0.1

Table 2

Sample	*Identification of phases*			*Heat treatment (ºC)*			
	Phase	Space Group	Nº PDF	1000	1100	1200	1300
$Y_4Al_2O_9$	$Y_4Al_2O_9$	P$2_1/c$	00-022-0987	100	100	52.7	35.0
	$YAlO_3$	P*bnm*	01-087-1288	-	-	36.4	47.8
	Y_2O_3	I*a-3*	01-074-1828	-	-	10.9	17.2
			χ^2	2.73	3.41	4.24	4.77
$Sm_4Al_2O_9$	$Sm_4Al_2O_9$	P$2_1/c$	00-029-0080	100	71.7	68.5	55.1
	$SmAlO_3$	P*bnm*	01-071-1597	-	18.0	20.4	27.7
	Sm_2O_3	C*2/m*	00-009-0201	-	10.3	6.6	17.2
	Sm_2O_3	I*a-3*	01-086-2479	-	-	4.5	-
			χ^2	2.33	2.19	1.91	1.67
$Eu_4Al_2O_9$	$Eu_4Al_2O_9$	P$2_1/c$	01-072-0682	100	96.3	100	100
	$EuAlO_3$	P*bnm*	00-009-0084	-	3.7	-	-
			χ^2	1.97	2.85	6.92	6.23
$Gd_4Al_2O_9$	$Gd_4Al_2O_9$	P$2_1/c$	00-030-0014	100	92.1	75.1	24.9
	$GdAlO_3$	P*bnm*	00-046-0395	-	7.9	15.6	41.8
	Gd_2O_3	C*2/m*	00-042-1465	-	-	9.3	33.3
			χ^2	1.97	2.19	2.93	2.74
$Tb_4Al_2O_9$	$Tb_4Al_2O_9$	P$2_1/c$	00-044-0221	100	90	3.1	1.3
	$TbAlO_3$	P*bnm*	00-024-1270	-	10	45.6	56.2
	Tb_2O_3	C*2/m*	01-074-2131	-	-	34.3	42.5
	Tb_2O_3	I*a-3*	01-086-2478	-	-	17.0	
			χ^2	1.94	3.18	4.23	3.29

Table 3.

Sample	*Identification of phases*			*At 1000 ºC*
	Phase	Space Group	Nº PDF	200 h
$Y_4Al_2O_9$	$Y_4Al_2O_9$	P*2₁/c*	00-022-0987	100
			χ^2	3.10
$Sm_4Al_2O_9$	$Sm_4Al_2O_9$	P*2₁/c*	00-029-0080	75.9
	$SmAlO_3$	P*bnm*	01-071-1597	14.8
	Sm_2O_3	C*2/m*	00-009-0201	9.3
			χ^2	2.33
$Eu_4Al_2O_9$	$Eu_4Al_2O_9$	P*2₁/c*	01-072-0682	97.0
	$EuAlO_3$	P*bnm*	00-009-0084	3.0
			χ^2	2.31
$Gd_4Al_2O_9$	$Gd_4Al_2O_9$	P*2₁/c*	00-030-0014	94.2
	$GdAlO_3$	P*bnm*	00-046-0395	5.8
			χ^2	2.09
$Tb_4Al_2O_9$	$Tb_4Al_2O_9$	P*2₁/c*	00-044-0221	93.4
	$TbAlO_3$	P*bnm*	00-024-1270	6.6
			χ^2	3.22

Table 4

Samples	*Initial V (Å³) at 30 ºC*	*V (Å³) of residue at 30 ºC*
$Y_4Al_2O_9$	831.5±0.1	831.1±0.1
$Sm_4Al_2O_9$	870.6±0.4	873.2±0.3
$Eu_4Al_2O_9$	857.3±0.2	847.5±0.3
$Gd_4Al_2O_9$	845.6±0.1	846.7±0.2
$Tb_4Al_2O_9$	834.0±0.2	835.3±0.6

Table 5

Compound	$\alpha_{300\text{-}1000\ ºC}$ *(1·10⁻⁶ K⁻¹)*
$Y_4Al_2O_9$	8.1
$Sm_4Al_2O_9$	9.0
$Eu_4Al_2O_9$	7.9
$Gd_4Al_2O_9$	7.7
$Tb_4Al_2O_9$	11.8